

Article

Image Quality Assessment for Digital Volume Correlation-Based Optical Coherence Elastography

Xianglong Lin ^{1,2} , Jinlong Chen ^{1,2}, Yongzheng Hu ^{1,2}, Xiaowei Feng ^{1,2}, Haosen Wang ^{1,2}, Haofei Liu ^{1,2} 
and Cuiru Sun ^{1,2,*} 

¹ Department of Mechanics, School of Mechanical Engineering, Tianjin University, Tianjin 300350, China

² Tianjin Key Laboratory of Modern Engineering Mechanics, Tianjin University, Tianjin 300350, China

* Correspondence: carry_sun@tju.edu.cn

Abstract: Optical coherence elastography (OCE) based on digital volume correlation (DVC) has the advantages of full 3D displacements and strain tensor quantification. However, the measurement results are often unreliable due to the poor quality of the optical coherence tomography (OCT) speckle patterns. This paper proposes an image evaluation index based on OCT-DVC (CMGG, combined mean attenuation intensity, breadth and dispersion of the gray level distribution), which comprehensively considers the OCT signals' attenuation and the breadth and dispersion of the gray level distribution of the OCT images. Virtual deformation experiments of phantoms by numerically applied displacements and deformation measurement of pork meat were conducted. The results of the mean bias errors have a corresponding good relationship with CMGG, which demonstrates the effectiveness of the proposed CMGG. Based on this index, a lot of time may be saved by a pretest evaluation during DVC-OCE measurement. CMGG also guides the development of OCE system design, adjustment and new DVC-OCE algorithms.

Keywords: optical coherent elastography; digital volume correlation; displacement; image evaluation index



Citation: Lin, X.; Chen, J.; Hu, Y.; Feng, X.; Wang, H.; Liu, H.; Sun, C. Image Quality Assessment for Digital Volume Correlation-Based Optical Coherence Elastography. *Photonics* **2022**, *9*, 573. <https://doi.org/10.3390/photonics9080573>

Received: 17 July 2022

Accepted: 11 August 2022

Published: 15 August 2022

Publisher's Note: MDPI stays neutral with regard to jurisdictional claims in published maps and institutional affiliations.



Copyright: © 2022 by the authors. Licensee MDPI, Basel, Switzerland. This article is an open access article distributed under the terms and conditions of the Creative Commons Attribution (CC BY) license (<https://creativecommons.org/licenses/by/4.0/>).

1. Introduction

Optical coherence elastography (OCE) has great potential for the early diagnosis of various diseases due to its high resolution in the mechanical characterization of biological tissue [1]. Speckle tracking by cross-correlation to obtain displacements and strains is the initial OCE method proposed in 1998 [2] and is widely used in ultrasound elastography [3,4]. Speckle correlation-based OCE methods have the advantage of simultaneous 2D or 3D deformation characterization over the phase-based OCE methods, which are usually effective in measuring the 1D deformation along the direction of the scanning beam only [5–7]. Digital volume correlation (DVC) is the most recent correlation-based OCE algorithm, which can obtain the full displacement and strain tensor in all directions [8]. However, the correlation status and the characteristics of the optical coherence tomography (OCT) speckle pattern directly influence the results of the DVC calculation. Low correlation between speckle patterns during deformation may result in measurement errors. Thus, it is important to qualify the OCT images before DVC calculation to ensure accurate deformation measurement results and to identify wrong results.

Most of the correlation algorithms used in OCE are directly borrowed from digital image correlation (DIC) or digital volume correlation (DVC). We previously calibrated a 2D OCE system based on the classical Newton–Raphson iteration DIC algorithm [5]. We found that with an OCT imaging depth of ~1 mm and a pretty long time of over 10 min, the correlation coefficient varies slightly, demonstrating that the time and imaging depth have a minor effect on the DIC calculation. The major factor that influences the correlation between the images is displacement. The correlation coefficient decreases with the displacement

increase. At ~1.5% strain, the correlation coefficient drops to 0.6. However, a quantitative evaluation of the measured strain maps was not conducted. In 2019, we developed an inverse compositional Gauss–Newton (IC-GN)-based DVC algorithm [9] and found that the maximum strain that can be measured accurately was only 0.6%. In addition, the correlation coefficient alone is not a good parameter to estimate the effectiveness of the results, as the values of the correlation coefficient change differently based on different calculation equations. Santamaría et al. [10] quantified the 3D strain caused by the chemical elastic effect in the arterial wall by using the DVC DaVis[®] (LaVision, Ypsilanti, MI, USA) software-based OCE. Speckle tracking-based OCE shows a great application prospect in biological tissue elastic imaging, such as skin, blood vessels, cornea, etc. [11–13]. However, the analysis and evaluation of the measurement accuracy are lacking. Applying the correlation algorithms directly without considering the quality of the OCT images during deformation may induce serious artifacts to the results.

The accuracy of the DVC method is influenced by many factors, such as the whole voxel and sub-voxel registration algorithm [14], shape function [15] and interpolation scheme selection [16]. In internal measurements where speckle cannot be prepared by manual operation, such as spraying, the image quality has become the primary issue affecting the accuracy of DVC. The speckle noise inherent in OCT images reduces the contrast of the image [17] and the clarity of the fine structures of biological tissues [18]. Many methods have been proposed to suppress the influence of noise and improve the resolution or contrast of OCT images [19–22]. Tyler et al. [23] have proved that when the position of the focal point of the light source is different from the density of the scatterer in the sample, the size and shape of the speckle pattern will also change. Numerical beam refocusing in OCT increases lateral resolution in the out-of-focus areas for strongly focused beams. Matveyev et al. [24] found that the numerical refocusing method may fail in the presence of scatterer motion. Although this processing has a good effect on boundary enhancement, the effect of this on the effective deformation information contained in speckles is not yet known. The evolution of the OCT speckle pattern induced by deformation was studied by Zaitsev et al. [25]. They found that the strain could induce OCT image speckle “blinking” and “boiling” due to the motion of scatterers. The significant distortion of the speckle pattern in the tissue leads to a strong increase in measurement errors. Thus, the criteria to evaluate the image quality to ensure correct correlation calculation is needed for speckle correlation-based OCE.

The size and distribution of speckles affect the accuracy of DIC and DVC results. There are several image quality evaluation criteria for the correlation calculation of incoherent images, such as mean intensity gradient (MIG), mean intensity of the second derivative (MIOSD) and mean subset fluctuation (MSF). MIG [26] reflects the contrast of the speckle pattern. MIOSD [27] reflects the smoothness of the gray surface of the speckle pattern. MSF reflects the influence of the speckle size and density [28]. However, these criteria are ineffective in laser speckle patterns, which generally do not have the high contrast and clear black and white dots as painted speckles. Song et al. proposed a Multi-Factor Fusion Index (MFFI) to assess the quality of laser speckle patterns for DIC [29]. MFFI can overcome the shortcoming of a single factor. However, only the gray information of the speckles is considered in the MFFI. In OCT imaging, under the assumption of linear polarization and a fully developed speckle pattern, the theoretical amplitude distribution of speckles obeys a Rayleigh distribution [30]. However, the amplitude distribution of speckles and the speckle size are determined by the focusing optics, the OCT resolution and the specimen’s microstructure. As the detailed optical properties of the biological tissue are not well known in most cases, the amplitude distribution of speckles is difficult to characterize [31]. Thus, new criteria are needed to evaluate the OCT images for speckle correlation-based OCE. The intensity in OCT images is usually displayed on the logarithmic scale [32], which displays the contrast variation of the grayscale of the OCT image [31]. The image contrast is also affected by the attenuation of the laser signal in biological tissues, caused by the absorption and scattering of the laser by the internal scatterers [33]. So, a global assessment

criterion combining gray level information of 3D OCT image and laser signal attenuation is necessary. The OCT image quality is affected by the parameters of the OCT system, such as the central wavelength of the laser source, the numerical aperture of the scanning lens and the laser intensity of the reference arm. It is necessary to propose an evaluation standard of OCT image quality and establish the relationship between different factors and the accuracy of the DVC-OCE method.

This study proposes an image evaluation index for OCT-DVC based on the characteristics of the OCT signal attenuation and gray level information for DVC-OCE process guidance. The attenuation characteristics of the OCT image, the breadth and dispersion characteristics of the OCT image gray level are comprehensively considered. Both simulation and phantom experiments of images demonstrated the effectiveness of the new image quality index. This index provides criteria for assessing whether the OCT images are suitable for DVC calculation. Based on this index, time will be saved from processing poor-quality images and the locations where the 3D displacements are not calculated accurately can be identified. It may also guide the optical system adjustment to improve OCT image quality and the determination of high-quality seed points for new DVC algorithm development.

2. Materials and Methods

2.1. DVC-Based OCE

Figure 1 is a schematic illustration of an experimental setup of the DVC-OCE system. The OCE system consists of a loading device and a swept-source OCT system (SSOCT) [9]. The laser light emitted from the swept laser (HSL-20-100-B, Santec, Aichi, Japan) goes to a coupler, 90% of the laser light is focused on the sample surface. In total, 10% of the laser enters the reference arm. The two beams of light pass through the circulator and enter the 50/50 coupler to interfere and be collected by a balanced photodetector (EBR370006-02, Exalos, Schlieren, Switzerland). A single laser signal can reconstruct a one-dimensional image of the sample (A-Scan). The galvanometer controls the laser movement in the X direction to obtain a 2D image (B-Scan). On this basis, the galvanometer controls the laser movement in the Y direction to reconstruct a three-dimensional image (C-Scan). The OCE system can obtain three-dimensional images of deformation under different loadings.

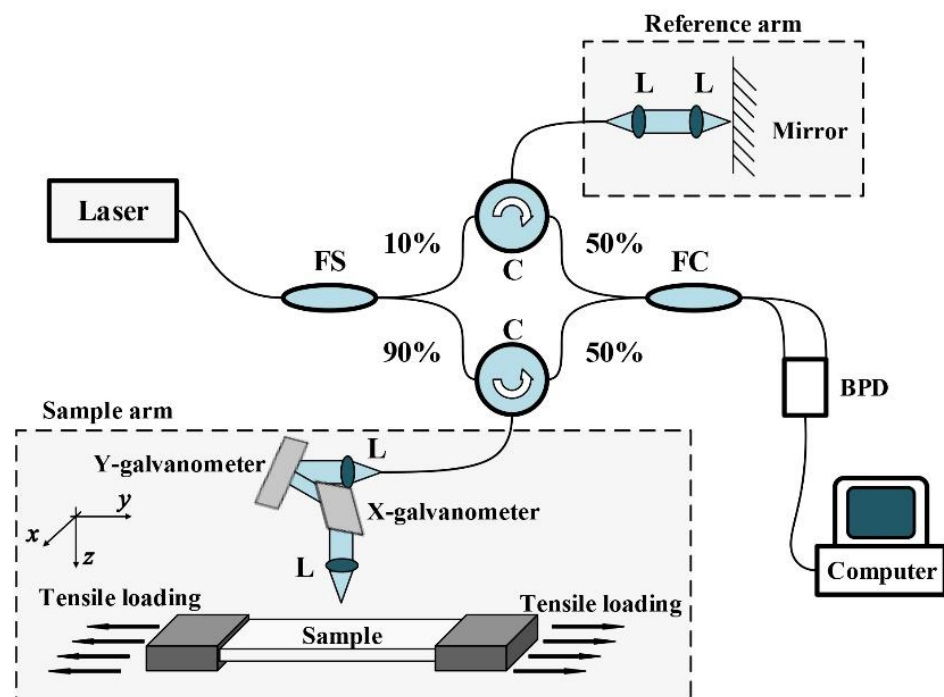


Figure 1. Schematic diagram of OCE system. FS, fiber splitter. FC, fiber coupler. BPD, balanced photodetector. L, lens. C, circulator.

The OCT signal is formed in the scattering medium by the coherent addition of multiple backscattered light fields. This causes a speckle phenomenon. The 3D OCT image has three resolutions. The features of the 3D OCT image are shown in Figure 2. Figure 2a shows the 3D OCT image reconstructed by the OCE system. Figure 2b shows the gray level distribution at the positions of 100, 200 and 300 voxels in the axial depth. It is found that the gray level distribution changes relatively coarsely. This is because the transverse section is composed of one voxel on a single A-Scan signal. Figure 2c represents an A-Scan image in a cross-section. The red dashed line represents the signal trend. It is found that the signal has not been attenuated. Figure 2d shows the gray level distribution at depths of 150, 300 and 450 voxels. It is found that the gray level distribution changes smoothly. This is because the axial section is composed of a complete single A-Scan. Figure 2e represents an A-Scan image on an axial section. The red dashed line represents the signal trend, and the signal is found to be attenuated.

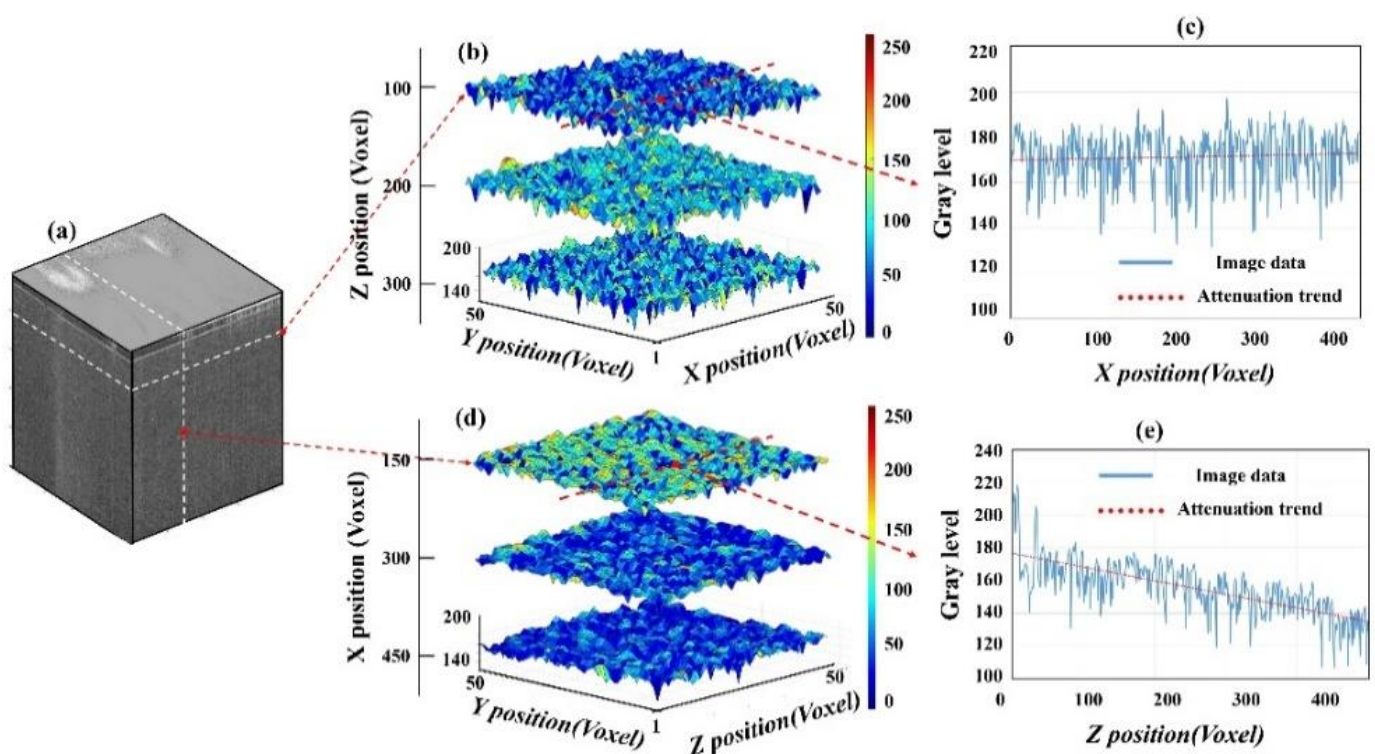


Figure 2. Features of 3D OCT image: (a) the 3D image reconstructed by the OCE system; (b) the gray level distribution at the positions of 100, 200 and 300 voxels in the axial depth; (c) A-Scan image in a cross-section; (d) the gray level distribution at the horizontal depth of 150, 300 and 450 voxels; (e) A-Scan image on an axial section.

The basic principle of the standard sub-block-based DVC method is shown in Figure 3. The DVC method is mainly based on the correlation calculation between the reference volume of interest (VOI) and the target VOI, where the gray value is assumed not to change before and after deformation. Figure 3 shows the matching of a reference block $f(x,y,z)$ and the block $g(x',y',z')$ after deformation for displacement calculation. This paper employs a coarse search step based on the full-search zero-mean normalized cross-correlation algorithm (ZNCC) correlation function and the inverse compositional Gauss–Newton (ICGN) DVC algorithm developed in our lab previously [9]. The 3D displacements can be obtained with sub-voxel resolution through the coarse–fine search DVC calculation.

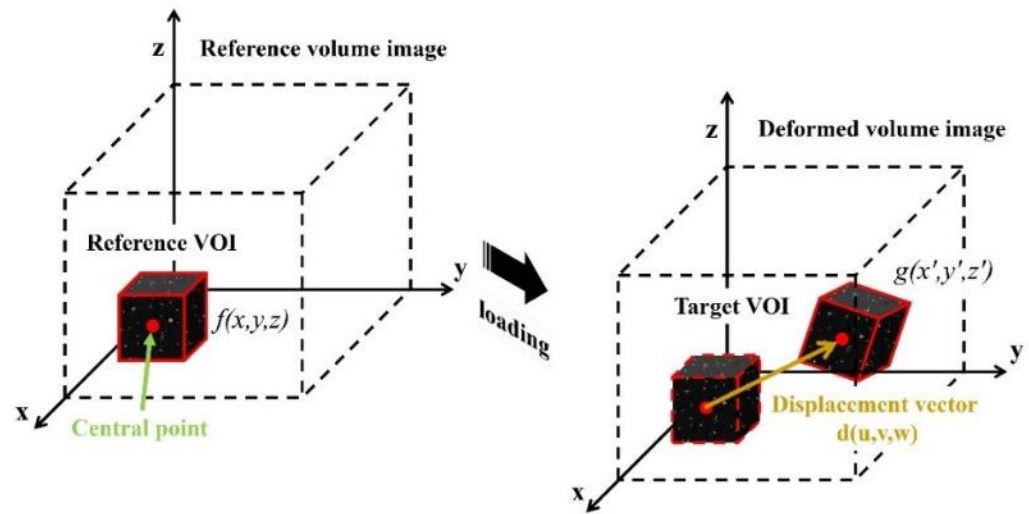


Figure 3. Diagram of finding the displacement by matching the 3D images before and after deformation by DVC.

The current DVC method obtains the strain field from the displacement field by a 3D pointwise least square fitting approach. The unknown polynomial coefficients $(a_i, b_i, c_i \ i = 0, 1, 2, 3)$ can be determined by minimizing the following least squares criteria.

$$\begin{cases} \chi^2(a_0, a_1, a_2, a_3) = \sum_{x,y,z \in W} [u(x, y, z) - a_0 + a_1x + a_2y + a_3z]^2 \\ \chi^2(b_0, b_1, b_2, b_3) = \sum_{x,y,z \in W} [v(x, y, z) - b_0 + b_1x + b_2y + b_3z]^2 \\ \chi^2(c_0, c_1, c_2, c_3) = \sum_{x,y,z \in W} [w(x, y, z) - c_0 + c_1x + c_2y + c_3z]^2 \end{cases} \quad (1)$$

where x, y and z are the local coordinates. u, v and w are the measured displacement fields. W is the set of valid data points in the local strain calculation box. The six Cauchy strain components at the interrogated point can be estimated as:

$$\begin{cases} \epsilon_{xx} = \frac{\partial u}{\partial x} = a_1, \epsilon_{yz} = \frac{1}{2} \left(\frac{\partial v}{\partial z} + \frac{\partial w}{\partial y} \right) = \frac{1}{2}(b_3 + c_2) \\ \epsilon_{yy} = \frac{\partial v}{\partial y} = b_2, \epsilon_{xz} = \frac{1}{2} \left(\frac{\partial u}{\partial z} + \frac{\partial w}{\partial x} \right) = \frac{1}{2}(a_3 + c_1) \\ \epsilon_{zz} = \frac{\partial w}{\partial z} = c_3, \epsilon_{xy} = \frac{1}{2} \left(\frac{\partial u}{\partial y} + \frac{\partial v}{\partial x} \right) = \frac{1}{2}(a_2 + b_1) \end{cases} \quad (2)$$

Therefore, the accuracy of the strain field in the DVC method depends on the calculation of the displacement field.

2.2. Quality Assessment of 3D OCT Images for DVC Calculation

According to the characteristics of the OCT signal, the SNR value is used to ensure the effectiveness of the region of interest. Due to the attenuation of the signal, the information carried by the image in the deep area has been masked by noise. SNR of the OCT image is defined [34] as follows:

$$\text{SNR} = 10 \log_{10} \left[\frac{\max(G^2)}{\delta^2} \right] \quad (3)$$

where G represents the gray value of the OCT image and δ^2 is the variance of the background noise region in the OCT image. The DVC calculation usually takes sub-block size $31 \times 31 \times 31$ voxels or more, so the local SNR value calculation along the axial depth and the in-region DVC calculation are performed with axial size 31 voxels and step size 5 voxels. In the system adopted in this paper, the area with a signal-to-noise ratio of more than 21 is

defined as the effective area by statistical analysis of multiple sets of specimens, and the image quality evaluation is carried out in the effective area image.

2.2.1. Mean Attenuation Intensity (MAI)

The laser transmission in biological tissues will be scattered or absorbed, which will change the laser’s intensity, coherence and polarization, resulting in the attenuation of the laser and affecting image quality. The signal attenuation will affect the mean deviation of the measured displacement. The global mean attenuation intensity parameter is proposed to evaluate the influence of the OCT signal, and its definition is in Equation (4), whose values range is 0–5.7, as shown in Figure 4.

$$\delta_{MAI} = a_{\mu} \cdot \frac{\sum_{j=1}^B \sum_{k=1}^C \mu_T(A_{jk})}{B \times C} \tag{4}$$

where $\mu_T(A_{jk}) = \mu_a(A_{jk}) + \mu_s(A_{jk})$ is the total attenuation of the A_{jk} -Scan signal of the j th B-scan and the k th C-Scan. The total attenuation of the signal considers both the attenuation of absorption $\mu_a(A_{jk})$ and the attenuation of scattering $\mu_s(A_{jk})$. a_{μ} is a linear constant. B and C are the numbers of B-Scan and C-Scan. Considering the effects of absorption and scattering, according to the Lambert–Beer law, the laser intensity with depth can be expressed as:

$$I = I_0^{-\mu_T z} \tag{5}$$

where I_0 is the integral constant and Z is the depth information of an A-Scan signal.

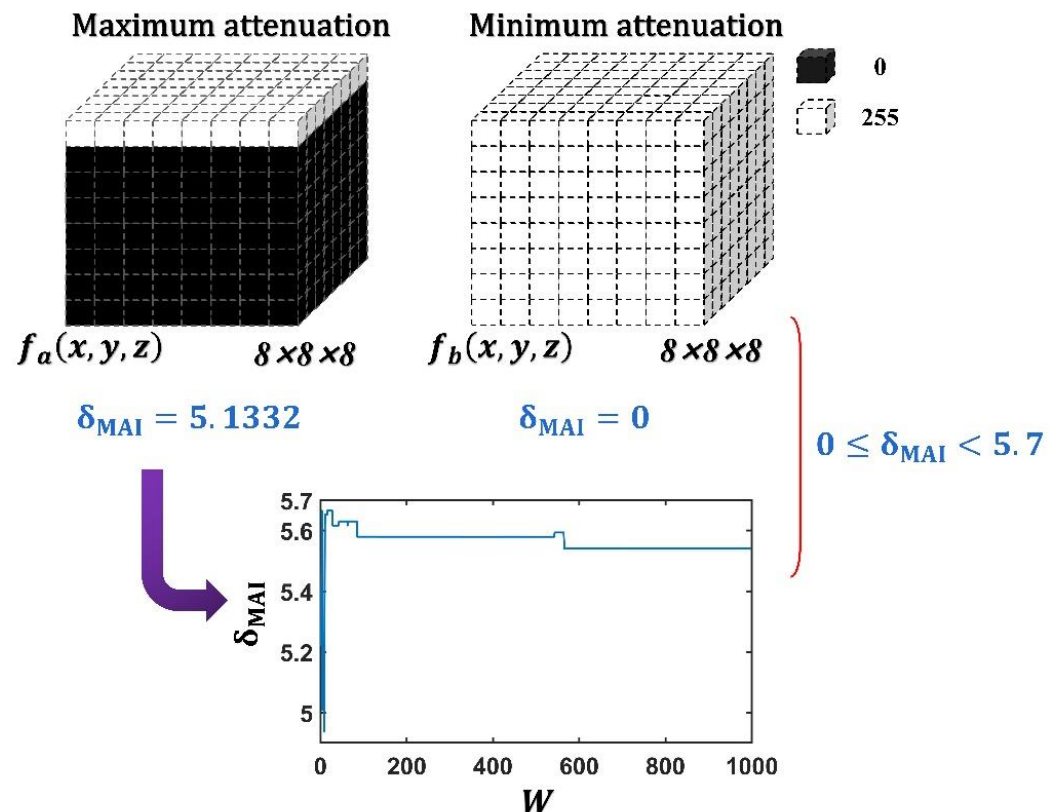


Figure 4. The principle of the value range of MAI: $f_a(x,y,z)$ is the schematic diagram of maximum OCT signal attenuation, $f_b(x,y,z)$ is the schematic diagram of minimum OCT signal attenuation.

2.2.2. Breadth and Dispersion of the Gray Level Distribution

The 3D OCT image comprises voxels with different gray levels, especially when imaged in heterogeneous tissue. Therefore, the characteristics of the gray level distribution may be a factor that influences DVC calculation. The gray level function of a 3D OCT

image is defined as $f(x, y, z)$. The gray distribution breadth (GDB) is defined as Equation (6) to evaluate the uniformity of the gray level distribution, whose value range is $\sqrt{L \times W \times H} \sim \sqrt{\frac{L \times W \times H}{256}}$.

$$\delta_{GDB} = \sqrt{\sum_{g=0}^{G-1} \frac{N_g^2}{L \times W \times H}} \tag{6}$$

where G represents the number of gray levels, N_g is the number counted when the number of gray levels is g , and L, W and H are the length, width and height of the 3D OCT image. GDB implies the coverage degree of the gray level number. The principle of GDB is shown in Figure 5. The size of the 3D image is $8 \times 8 \times 8$ voxels. There are different breadths of gray level distribution in $f_a(x, y, z)$, $f_b(x, y, z)$ and $f_c(x, y, z)$. Additionally, the wider the gray level contained in the OCT image and the more uniform the distribution, the smaller the value of GDB.

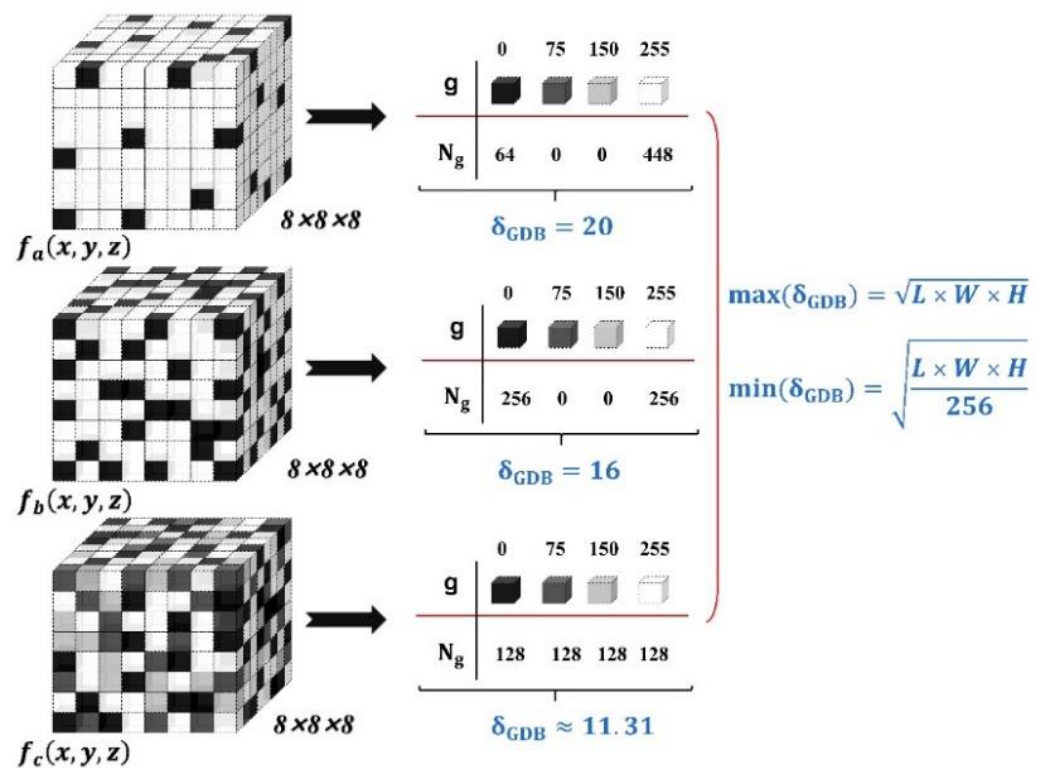


Figure 5. The principle of GDB: $f_a(x, y, z)$, $f_b(x, y, z)$ and $f_c(x, y, z)$ are the schematic diagram corresponding to δ_{GDB} 20, 16, 11.31.

The contrast of the OCT image can affect the extraction of useful information. The dispersion of the gray level distribution can express the contrast of the image, that is, the dispersion of the gray level distribution in the image relative to the mean gray level value of the image. The OCT image gray distribution dispersion index (GDD) is proposed as Equation (7), whose value range is $0 \sim \sqrt{127.5}$.

$$\delta_{GDD} = \sqrt{\sum_{g=0}^{G-1} \left\{ (g - |P|)^2 \times \frac{N_g}{L \times W \times H} \right\}} \tag{7}$$

where $|P| = \sum_{g=0}^{G-1} \frac{g \times N_g}{L \times W \times H}$ is the mean value of the gray level. Figure 6 shows the principle of GDD. The size of the 3D image is $8 \times 8 \times 8$ voxels. There are different dispersions of gray level distribution in $f_a(x, y, z)$, $f_b(x, y, z)$ and $f_c(x, y, z)$, and the more concentrated the gray

level distribution of the OCT image is, the worse the image contrast and the greater the value of GDD.

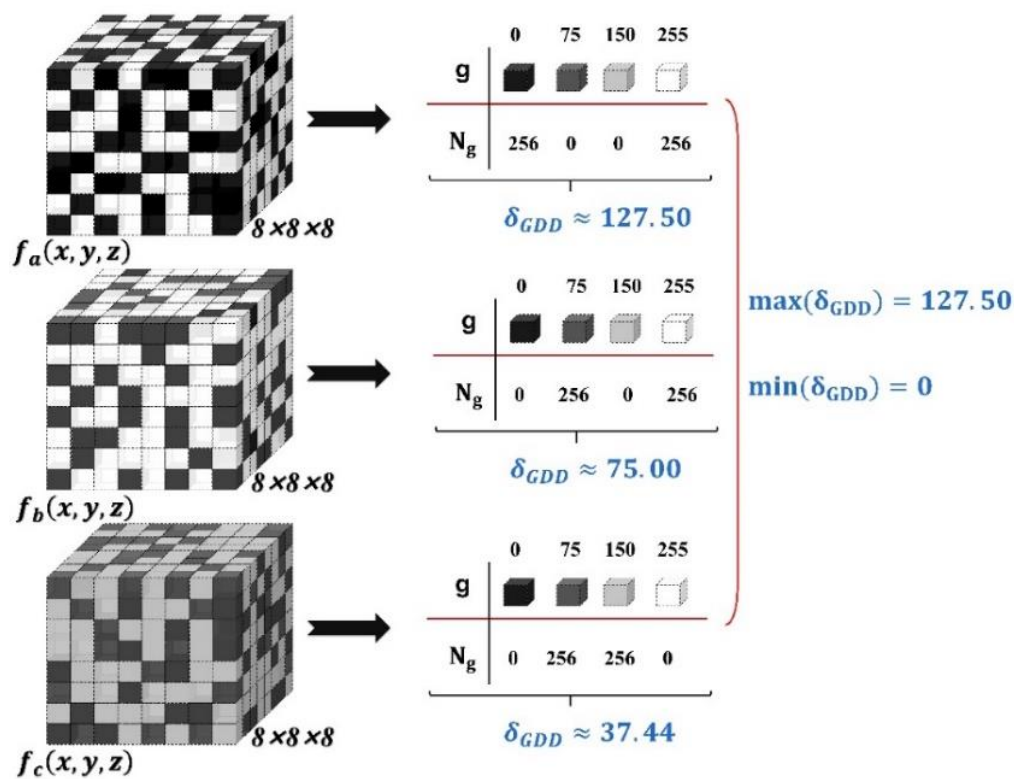


Figure 6. The principle of GDD: $f_a(x,y,z)$, $f_b(x,y,z)$ and $f_c(x,y,z)$ are the schematic diagram corresponding to δ_{GDD} 127.50, 75.00, 37.44.

2.2.3. Image Evaluation Index Based on OCT-DVC

To combine the MAI, GDB and GDD, we propose an integrated parameter CMGG (combined MAI, GDB, and GDD) for the image evaluation index based on OCT-DVC, as:

$$\delta_{CMGG} = a \cdot \frac{\delta_{MAI} \cdot \delta_{GDD}}{\delta_{GDB}} \tag{8}$$

where a is a linear constant. The value range of δ_{CMGG} is $0 \sim \frac{726.75}{\sqrt{L \times W \times H}}$. The value range of the three parameters is not in the order of magnitude, and the linear constant is set to adjust the order of magnitude of δ_{CMGG} .

2.3. Mean Bias Error

The displacement obtained by the DVC method is compared with the applied displacement to evaluate the influence of CMGG on the calculation results. The mean bias error (E_m) is used to evaluate the error in calculating displacement.

$$E_m = \frac{\sum_{i=1}^N u_i}{N} - u_r \tag{9}$$

where N is the number of sub-voxels, u_i is estimated sub-voxel displacement and u_r is the actual sub-voxel displacement.

3. Results

3.1. Verification Experiment of Reference Arm Adjustment

The histogram of the OCT image is influenced by the light intensity of the reference arm. A phantom with scatterers (20 nm, 0.5%) was imaged when the power of the reference

arm was adjusted. In the system of this study, the reference arm power is regulated by controlling the attenuator through a hexadecimal serial port. When the reference power is higher than 95.71 μW (i.e., the parameter of serial port is lower than 8), it masks the signal of the sample arm signal. When the reference power is lower than 2.91 μW (i.e., the parameter of serial port is higher than B) it attenuates the signal of the sample arm. When the power of the reference arm was adjusted from 95.71 μW to 2.91 μW with random steps, OCT images taken are shown in Figure 7. The 3D OCT images were sub-voxel shifted in the Fourier domain [16] along the X-scan direction and the depth direction to obtain corresponding deformed OCT images. Since the X-scan direction and the Y-scan direction of the 3D OCT image have the same characteristics, only the X-scan direction is investigated in this paper. The translation range is 0–1 voxel, and the translation step is 0.1 voxel. The displacement of the deformed 3D OCT image relative to that before the deformation is calculated by the 3D IC-GN DVC method.

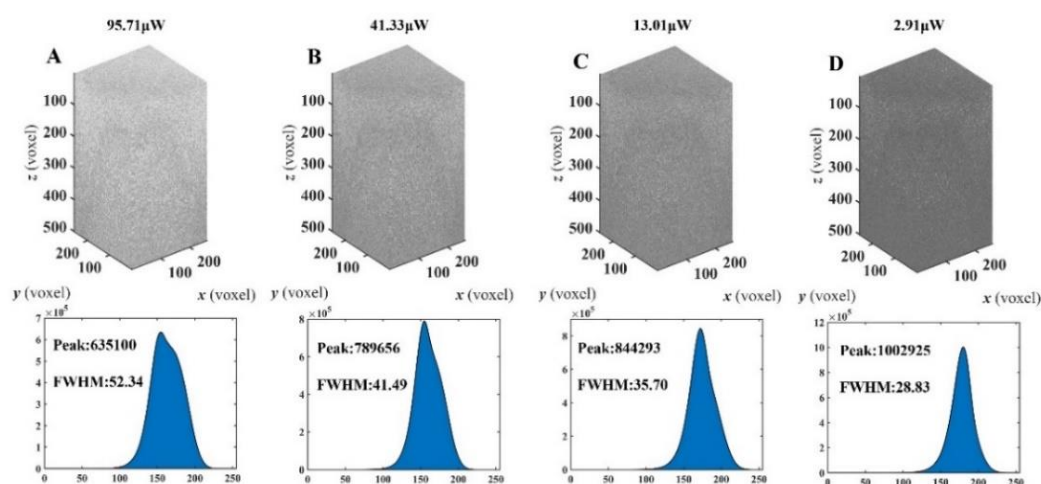


Figure 7. OCT images (A–D) with different reference arm light intensities (95.71 μW , 41.33 μW , 13.01 μW , 2.91 μW) and the corresponding histograms.

Figure 8 shows the influence of different reference arm laser intensities based on CMGG. Figure 8a,b are the sub-voxel displacements’ mean bias errors. It shows that the mean bias errors are a sinusoidal function of the applied displacement with approximately 1 voxel period. This sinusoidal distribution error is caused by the sub-voxel interpolation algorithm [15]. It can be seen that the mean bias errors of sub-voxel displacement in the depth direction shown in Figure 8b are overall lower than those in the X direction shown in Figure 8a. Figure 8c shows the OCT image quality parameters MAI, GDD, GDB and CMGG versus reference arm laser intensity. When CMGG decreases, the mean bias errors of the OCT images on the voxel displacement in the depth direction and X direction become larger. The quality of OCT image D, i.e., the reference arm laser intensity is 2.91 μW , is the lowest, and the mean bias error is the largest. In OCT images A and B, there is little difference in mean bias errors. MAI, GDD and GDB have no obvious monotonicity as a whole. Considering the gray image distribution and the attenuation of OCT signal alone is not enough to evaluate the image quality. The correlation is analyzed with Statistical Package for Social Science 25 (SPSS). The Pearson correlation coefficient for δ_{CMGG} and the mean bias errors of displacement was -0.964^{**} Sig. (two-tailed) < 0.01 , showing a significant negative correlation.

3.2. Verification Experiment of Phantoms with Different Scatterers

When the power of the reference arm is set as 95.71 μW . Silica gel phantoms with different sizes and mass fractions of scatterers (Titanium dioxide, TiO_2 , Shanghai Macklin Biochemical Co., Ltd., Shanghai, China) were imaged. The preparation process of the silica gel sample is briefly as follows, type AB liquid silica gel is mixed in a ratio of 1:1 and TiO_2

particles are added as a scattering agent. After being fully stirred, the mixture is poured into a Petri dish. Air bubbles are removed in a vacuum chamber. Four types of phantoms were made with TiO₂ particles. Scatterer parameters and OCT images with the histograms of the phantoms are shown in Figure 9. It shows the phantom without particles had the lowest FWHM and the largest peak. The content decrease for particles of the same size will reduce FWHM, and the corresponding peak will increase. This means that the sharper gray level distribution may have less useful information. Larger-sized particles increase FWHM and peak.

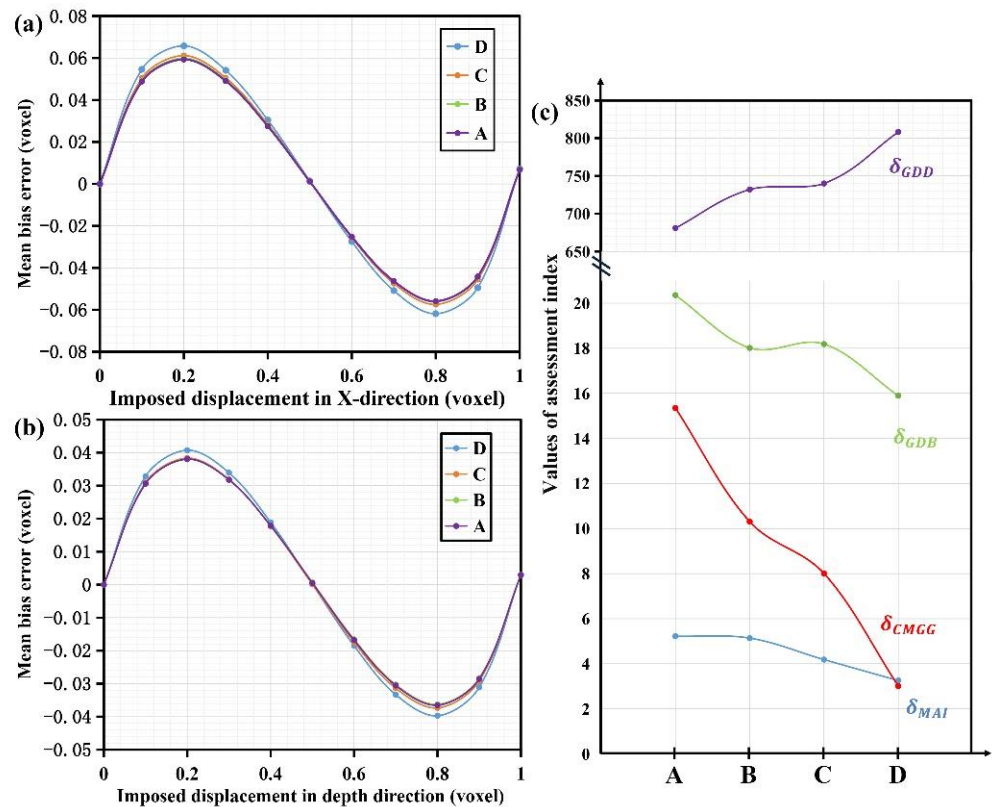


Figure 8. The influence of different reference arm laser intensities based on CMGG. (a) Mean bias errors of imposed displacement in X direction. (b) Mean bias errors of imposed displacement in depth direction. (c) Evaluation index of OCT image under different reference arm laser intensities.

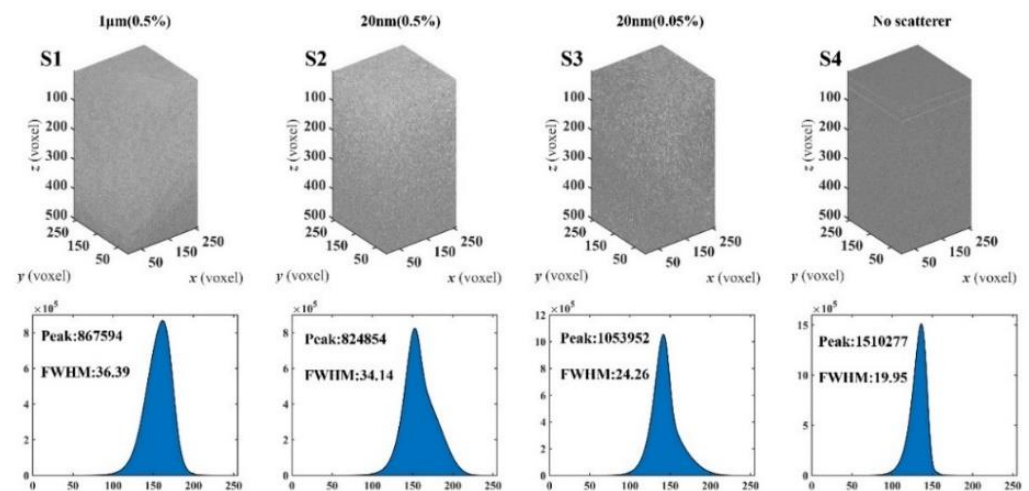


Figure 9. Three-dimensional OCT images of silica gel phantoms with different sizes and mass fractions of scatterers and their corresponding histograms of phantoms. S1: 1 μm (0.5%), S2: 20 nm (0.5%), S3: 20 nm (0.05%), S4: No scatterer.

Virtual deformation was applied similarly to Section 3.1. The DVC calculated displacements. Figure 10 shows the mean bias errors of the displacement and the image quality indices. Figure 10a,b show that the mean bias errors of sub-voxel displacement in the depth direction are overall lower than those in the X direction. Figure 10c shows that the mean bias errors of the sub-voxel displacement in the depth direction and X direction of the OCT image will increase with the decrease in CMGG. It can be seen that when the value of CMGG is the largest, S2 has the smallest mean bias error along the X direction and depth direction. When the value of CMGG is the smallest, S4 has the smallest mean bias error along the X and depth directions. CMGG of S3 is greater than S1, and the mean bias errors of S3 along the X direction and depth direction are less than S1. A single OCT image quality evaluation parameter cannot express the above phenomenon. The Pearson correlation coefficient for δ_{CMGG} and the mean bias errors of displacement was -0.875^{**} Sig. (two-tailed) < 0.01 , showing a significant negative correlation.

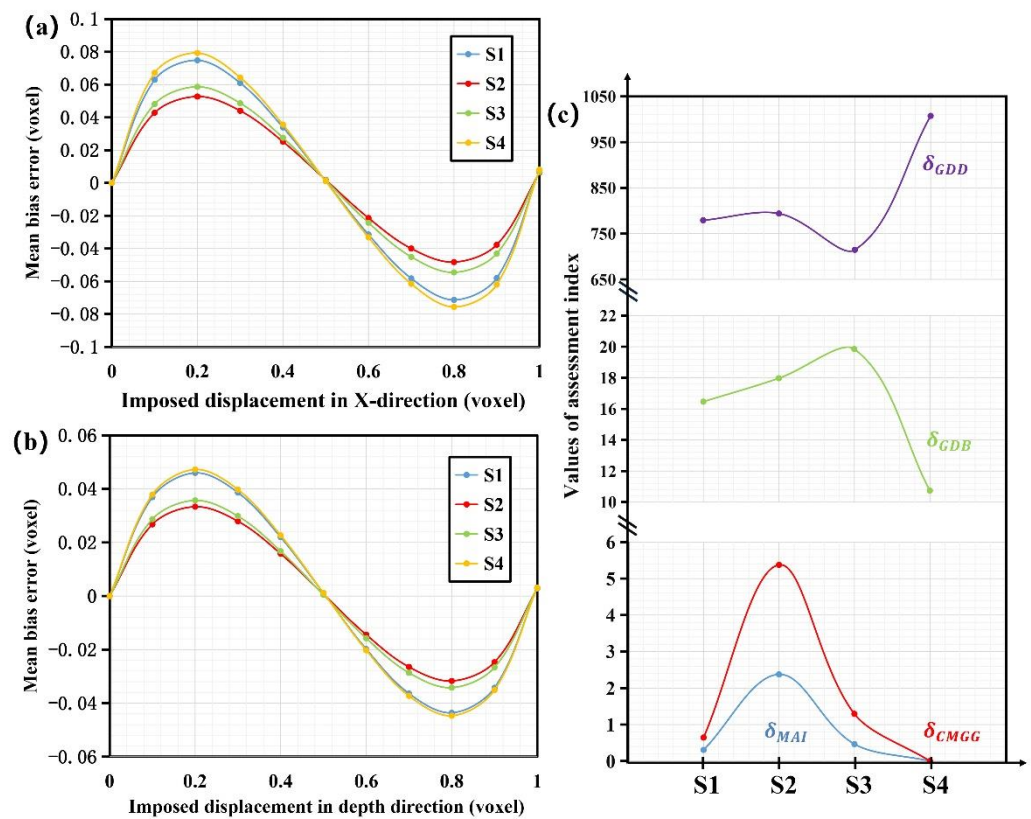


Figure 10. The verification result is based on CMGG. (a) Mean bias errors of imposed displacement in X direction. (b) Mean bias errors of imposed displacement in depth direction. (c) Evaluation index of OCT image with different contents of scatterers.

3.3. The Criteria Evaluation in Deformation Measurement of Pork Sample

A compressional experiment of pork samples was conducted. A cubic pork specimen was cut from the pork meat bought from the local supermarket and fixed in a homemade compressional loading device. The loading device consists of a glass window which allows the OCT beam to pass through, a load cell at the bottom measuring the load applied and a translation stage with high precision providing the scale of compression. A reference 3D OCT image was taken when 0.620 N preload was applied, and a deformed 3D OCT image was taken when the pork specimen was compressed by 30 μm . The Young’s modulus of the pork was 123.9 kPa, measured by tensile testing. Details of the experiments can be found in our previous study [35]. The reference 3D volume OCT is shown in Figure 11a. The region of interest was divided into six parts to evaluate the image quality, as shown in Figure 11a. In each part, the quality index is calculated for 81 points, 9×9 points in the x

and y directions. CMGG in different areas is shown in Figure 11b. It can be seen that CMGG of Part I is the largest. With the increase in depth, CMGG decreases. The displacement w field and strain ϵ_{zz} field along the z direction are shown in Figure 11c,e. The mean bias errors of the displacements and strain of 81 points in different parts along the z direction are plotted in Figure 11d,f. The mean bias errors increase when it drops to about 4 at part IV. CMGG of Part VI is the lowest, and the mean bias errors of this part are the largest.

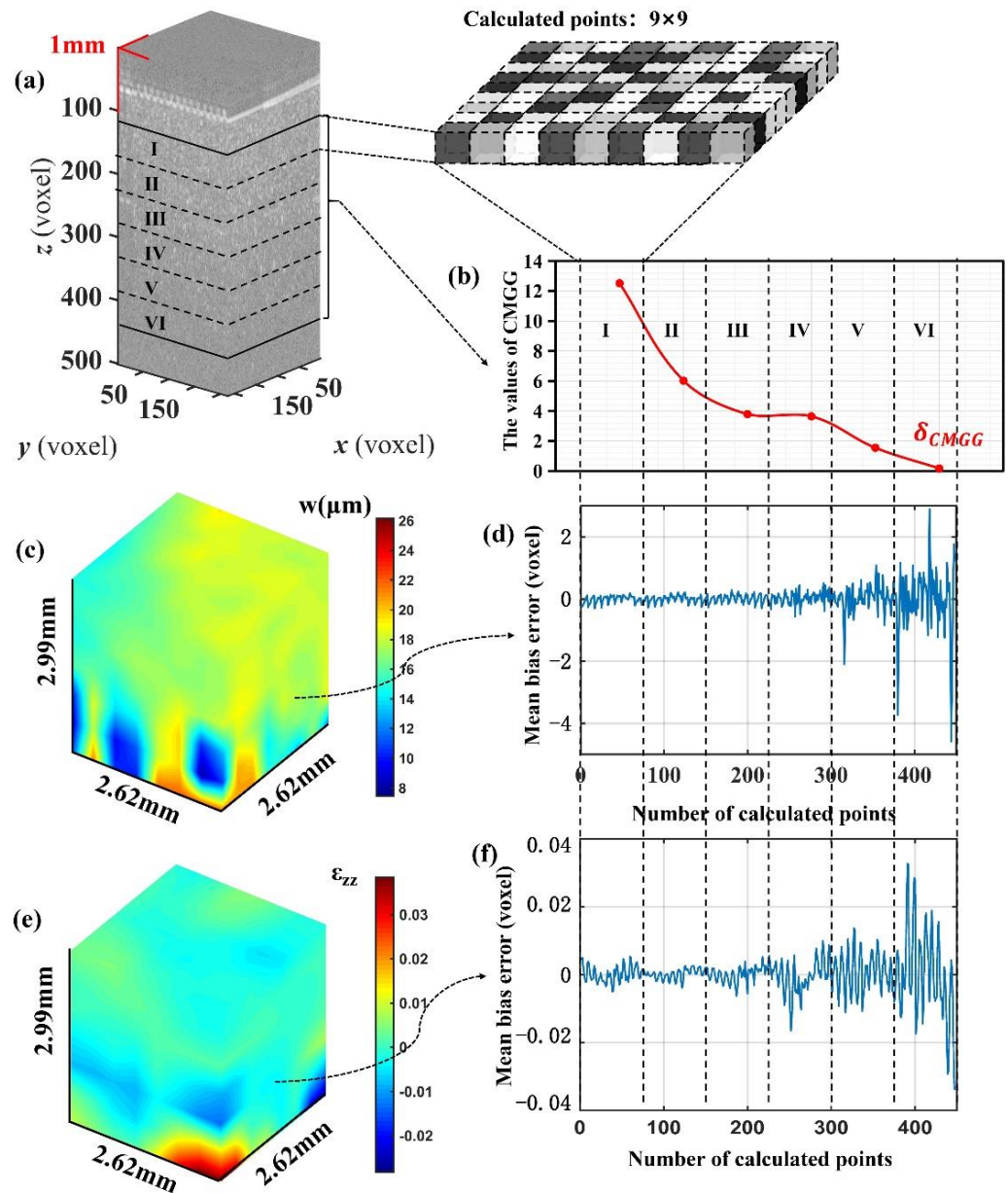


Figure 11. The criteria evaluation in deformation measurement. (a) Three-dimensional OCT image of a piece of pork. (b) CMGG in different areas. (c) The displacement w field along the z direction. (d) The mean bias errors of the displacements of 81 points in different parts along the z direction. (e) the strain ϵ_{zz} field along the z direction. (f) The mean bias errors of the strains of 81 points in different parts along the z direction.

4. Discussion

The virtual deformation experiments shown in Figure 10 and the actual deformation experiments shown in Figure 11 demonstrate the effectiveness of CMGG proposed in this paper. To further demonstrate the advantage of CMGG over existing quality assessment criteria for OCT speckle patterns, the MIG, MIOSD and MSF of phantoms with different

scatterers are plotted in Figure 12. It shows that the MIG, MIOSD and MSF at the 3D level have almost no corresponding relationship with the change in the mean bias errors. Therefore, the OCT images capable of DVC calculation cannot be distinguished based on these parameters. A higher CMGG indicates a good quality OCT image. The OCT image with high δ_{CMGG} is good for DVC calculation to obtain accurate displacements and strains.

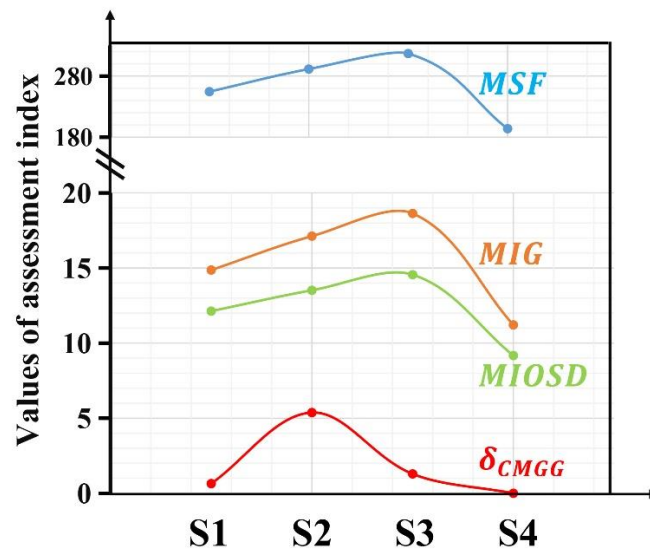


Figure 12. Comparison of different assessment criteria.

By comparing CMGG in Figures 8, 10 and 11, it was found that different influences on the quality of OCT images lead to changes in CMGG. CMGG is a multi-factor index. The speckle pattern of an OCT image contains a lot of information. The contrast of the OCT image depends on the amount of laser attenuation through the scatterer. As shown in Figure 4, when no attenuation of the OCT signal occurs ($MAI = 0$), there is only one gray level in the OCT image and it is spread out globally, which is not applicable to the DVC calculation at all. On the other hand, when the maximum attenuation of the OCT signal occurs (MAI reaches its maximum value), there are two extreme gray levels in the OCT image, but due to the concentrated distribution of gray levels, this situation is also not applicable to the DVC calculation. Therefore, GDD and GDB parameters are needed to evaluate the OCT image quality in cooperation. A high-quality OCT image should occupy all possible grayscales and be evenly distributed, expressed as a smaller GDB. In contrast, the distribution of these grayscales should be more dispersed, which is expressed as a larger GDD. When the image quality caused by different factors is studied, CMGG is stabilized at the same order of magnitude level through the linear coefficient a in Equation (6), which is convenient to reflect the influence of research factors intuitively. However, when more complex factors affect OCT image quality, CMGG needs to be unified, which is a limitation of the current research. In the future, we will further study and give a more general modulation method for CMGG to evaluate the OCT image quality caused by complex influencing factors.

Figures 8a and 10a show that the mean bias errors change sinusoidally with the sub-voxel displacement, which is due to the sub-voxel interpolation of gray value and gray value gradient [36]. The amplitude comparison of the sinusoidal curve can distinguish the calculation error caused by the image quality. However, the OCT image quality standard cannot evaluate speckle decorrelation when large deformation occurs. As shown in Figure 10, CMGG seems to be a useful tool for DVC measurement based on OCT images when decorrelation can be avoided or ignored.

The assessment of OCT image quality by CMGG can avoid unreliable final findings due to a blind OCE-DVC calculation. Figure 11 shows the variation in the accuracy of the DVC calculation versus CMGG during an actual biological tissue measurement. It can be

seen that when δ_{CMGG} is ≥ 4 , the DVC measurement is accurate. Thus, 4 is the threshold value to determine whether a sub-volume is good enough for DVC processing for this specific experiment. However, more experiments and in-depth analysis are required to determine whether the value of 4 is applicable to DVC-OCE experiments of various tissue.

The light intensity of the OCT system's reference arm influences the OCT images' noise levels and the DVC calculation's accuracy. The results shown in Figure 8 indicate that CMGG can be used to guide the parameter adjustment of the OCT system to ensure the most appropriate reference light intensity. Other system parameters including the scanning lens's numerical aperture and the sample arm's focal position can also be adjusted simultaneously under the guidance of CMGG to obtain the best images for further DVC processing [37]. Calculation of DVC typically takes tens of hours. The parallel DVC computing algorithm is one of the hot research topics for improving DVC efficiency. A run of the OCT image quality test proposed in this study only takes several minutes, which may provide an effective method for high-quality seed point determination in the parallel algorithm.

5. Conclusions

This paper proposes a new, simple and effective global parameter called CMGG, combining the global mean attenuation intensity, the breadth and dispersion of grayscale distribution and other influencing factors. The numerical sub-voxel translation is carried out for phantom with different reference arm conditions and parameters to verify the correctness and effectiveness of the new parameters. The results show that the mean bias errors of the measured displacement are closely related to CMGG. The larger the CMGG, the smaller the mean bias errors produced by the OCT image. Therefore, the so-called good OCT image should have a large CMGG. This paper further verifies the validity of the index by biological tissue deformation measurements and shows that the index can evaluate errors before deformation measurements. The evaluation index is expected to be used in the DVC algorithm and OCE system optimization.

Author Contributions: Conceptualization, J.C. and X.L.; methodology, X.L.; software, Y.H.; validation, X.L. and C.S.; investigation, X.L. and H.W.; writing—review and editing, X.L., H.L., X.F. and C.S.; funding acquisition, J.C. and C.S. All authors have read and agreed to the published version of the manuscript.

Funding: The work was supported by the National Natural Science Foundation of China (Nos. 11972249, 11872267, 11890680, 12021002) and Tianjin Science and Technology Planning Project (No. 20jczdj00760).

Institutional Review Board Statement: Not applicable.

Informed Consent Statement: Not applicable.

Data Availability Statement: Available upon request.

Acknowledgments: The authors would like to thank the editors and anonymous reviewers for giving valuable suggestions that have helped to improve the quality of the manuscript.

Conflicts of Interest: The authors declare no conflict of interest.

References

1. Wang, S.; Larin, K.V. Optical coherence elastography for tissue characterization: A review. *J. Biophotonics* **2015**, *8*, 279–302. [[CrossRef](#)] [[PubMed](#)]
2. Schmitt, J. OCT elastography: Imaging microscopic deformation and strain of tissue. *Opt. Express* **1998**, *3*, 199–211. [[CrossRef](#)] [[PubMed](#)]
3. Ophir, J.; Céspedes, I.; Ponnekanti, H.; Yazdi, Y.; Li, X. Elastography: A Quantitative Method for Imaging the Elasticity of Biological Tissues. *Ultrasound Imaging* **1991**, *13*, 111–134. [[CrossRef](#)]
4. Parker, K.J.; Doyley, M.M.; Rubens, D.J. Corrigendum: Imaging the elastic properties of tissue: The 20 year perspective. *Phys. Med. Biol.* **2012**, *57*, 5359–5360. [[CrossRef](#)]
5. Sun, C.; Standish, B.; Vuong, B.; Wen, X.Y.; Yang, V. Digital image correlation-based optical coherence elastography. *J. Biomed. Opt.* **2013**, *18*, 121515. [[CrossRef](#)] [[PubMed](#)]

6. Fu, J.; Pierron, F.; Ruiz, P.D. Elastic stiffness characterization using three-dimensional full-field deformation obtained with optical coherence tomography and digital volume correlation. *J. Biomed. Opt.* **2013**, *18*, 121512. [[CrossRef](#)]
7. Zaitsev, V.Y.; Matveyev, A.L.; Matveev, L.A.; Sovetsky, A.A.; Hepburn, M.S.; Mowla, A.; Kennedy, B.F. Strain and elasticity imaging in compression optical coherence elastography: The two-decade perspective and recent advances. *J. Biophotonics* **2021**, *14*, e202000257. [[CrossRef](#)]
8. Larin, K.V.; Sampson, D.D. Optical coherence elastography-OCT at work in tissue biomechanics [Invited]. *Biomed. Opt. Express* **2017**, *8*, 1172–1202. [[CrossRef](#)]
9. Meng, F.; Chen, C.; Hui, S.; Wang, J.; Feng, Y.; Sun, C. Three-dimensional static optical coherence elastography based on inverse compositional Gauss-Newton digital volume correlation. *J. Biophotonics* **2019**, *12*, e201800422. [[CrossRef](#)]
10. Santamaría, V.A.A.; Garcia, M.F.; Molimard, J.; Avril, S. Characterization of chemoelastic effects in arteries using digital volume correlation and optical coherence tomography. *Acta Biomater.* **2020**, *102*, 127–137. [[CrossRef](#)]
11. Liu, P.; Groves, R.M.; Benedictus, R. Optical coherence elastography for measuring the deformation within glass fiber composite. *Appl. Opt.* **2014**, *53*, 5070–5077. [[CrossRef](#)] [[PubMed](#)]
12. Fu, J.; Haghighi-Abayneh, M.; Pierron, F.; Ruiz, P.D. Depth-Resolved Full-Field Measurement of Corneal Deformation by Optical Coherence Tomography and Digital Volume Correlation. *Exp. Mech.* **2016**, *56*, 1203–1217. [[CrossRef](#)]
13. Midgett, D.E.; Quigley, H.A.; Nguyen, T.D. In vivo characterization of the deformation of the human optic nerve head using optical coherence tomography and digital volume correlation. *Acta Biomater.* **2019**, *96*, 385–399. [[CrossRef](#)]
14. Ge, H.; He, Y.; Shen, L.; Liu, D.; Zhang, B.; Guo, S. Digital image frequency spectrum method for analyzing speckle displacement in frequency domain. *Opt. Lett.* **2015**, *40*, 942–945. [[CrossRef](#)] [[PubMed](#)]
15. Schreier, H.W.; Sutton, M.A. Systematic errors in digital image correlation due to undermatched subset shape functions. *Exp. Mech.* **2002**, *42*, 303–310. [[CrossRef](#)]
16. Schreier, H.; Braasch, J.; Sutton, M. Systematic errors in digital image correlation caused by intensity interpolation. *Opt. Eng.* **2000**, *39*, 2915–2921. [[CrossRef](#)]
17. Gossage, K.W.; Smith, C.M.; Kanter, E.M.; Hariri, L.P.; Stone, A.L.; Rodriguez, J.J.; Williams, S.K.; Barton, J.K. Texture analysis of speckle in optical coherence tomography images of tissue phantoms. *Phys. Med. Biol.* **2006**, *51*, 1563–1575. [[CrossRef](#)]
18. Pan, Y.; Birngruber, R.; Engelhardt, R. Contrast limits of coherence-gated imaging in scattering media. *Appl. Opt.* **1997**, *36*, 2979–2983. [[CrossRef](#)]
19. Bashkansky, M.; Reintjes, J. Statistics and reduction of speckle in optical coherence tomography. *Opt. Lett.* **2000**, *25*, 545–547. [[CrossRef](#)]
20. Ifthimia, N.; Bouma, B.E.; Tearney, G.J. Speckle reduction in optical coherence tomography by path length encoded angular compounding. *J. Biomed. Opt.* **2003**, *8*, 260. [[CrossRef](#)]
21. Rogowska, J.; Bryant, C.M.; Brezinski, M.E. Cartilage thickness measurements from optical coherence tomography. *J. Opt. Soc. Am. A* **2003**, *20*, 357–367. [[CrossRef](#)] [[PubMed](#)]
22. Pircher, M.; Gotzinger, E.; Leitgeb, R.; Fercher, A.F.; Hitzinger, C.K. Speckle reduction in optical coherence tomography by frequency compounding. *J. Biomed. Opt.* **2003**, *8*, 565–569. [[CrossRef](#)] [[PubMed](#)]
23. Tyler, S.; Ralston, Daniel, L.; Marks, Scott, P.; Carney, Stephen, A.; Boppart. Real-time interferometric synthetic aperture microscopy. *Opt. Express* **2008**, *16*, 4. [[CrossRef](#)]
24. Matveyev, A.L.; Matveev, L.A.; Moiseev, A.A.; Sovetsky, A.A.; Gelikonov, G.V.; Zaitsev, V.Y. Semi-analytical full-wave model for simulations of scans in optical coherence tomography with accounting for beam focusing and the motion of scatterers. *Laser Phys. Lett.* **2019**, *16*, 085601. [[CrossRef](#)]
25. Zaitsev, V.Y.; Matveyev, A.L.; Matveev, L.A.; Gelikonov, G.V.; Gelikonov, V.M.; Vitkin, A. Deformation-induced speckle-pattern evolution and feasibility of correlational speckle tracking in optical coherence elastography. *J. Biomed. Opt.* **2015**, *20*, 75006. [[CrossRef](#)]
26. Pan, B.; Lu, Z.; Xie, H. Mean intensity gradient: An effective global parameter for quality assessment of the speckle patterns used in digital image correlation. *Opt. Lasers Eng.* **2010**, *48*, 469–477. [[CrossRef](#)]
27. Yu, H.; Guo, R.; Xia, H.; Yan, F.; Zhang, Y.; He, T. Application of the mean intensity of the second derivative in evaluating the speckle patterns in digital image correlation. *Opt. Lasers Eng.* **2014**, *60*, 32–37. [[CrossRef](#)]
28. Bomarito, G.F.; Hochhalter, J.D.; Ruggles, T.J.; Cannon, A.H. Increasing accuracy and precision of digital image correlation through pattern optimization. *Opt. Lasers Eng.* **2017**, *91*, 73–85. [[CrossRef](#)]
29. Song, J.; Yang, J.; Liu, F.; Lu, K. Quality assessment of laser speckle patterns for digital image correlation by a Multi-Factor Fusion Index. *Opt. Lasers Eng.* **2020**, *124*, 105822. [[CrossRef](#)]
30. Karamata, B.; Hassler, K.; Laubscher, M.; Lasser, T. Speckle statistics in optical coherence tomography. *J. Opt. Soc. Am. A* **2005**, *22*, 593–596. [[CrossRef](#)]
31. Armitage, J.; Lamouche, G.; Vergnole, S.; Bisailon, C.E.; Dufour, M.; Maciejko, R.; Monchalain, J.P. Speckle size in optical Fourier domain imaging. In *Photonics North*; SPIE: Bellingham, DC, USA, 2007.
32. Lee, P.; Gao, W.; Zhang, X. Speckle properties of the logarithmically transformed signal in optical coherence tomography. *J. Opt. Soc. Am. A* **2011**, *28*, 517–522. [[CrossRef](#)] [[PubMed](#)]

33. Gong, P.; Almasian, M.; van Soest, G.; de Bruin, D.; van Leeuwen, T.; Sampson, D.; Faber, D. Parametric imaging of attenuation by optical coherence tomography: Review of models, methods, and clinical translation. *J. Biomed. Opt.* **2020**, *25*, 040901. [[CrossRef](#)] [[PubMed](#)]
34. Puvanathan, P.; Bizheva, K.J.O.E. Interval type-II fuzzy anisotropic diffusion algorithm for speckle noise reduction in optical coherence tomography images. *Opt. Express* **2009**, *17*, 733–746. [[CrossRef](#)] [[PubMed](#)]
35. Meng, F.; Zhang, X.; Wang, J.; Li, C.; Chen, J.; Sun, C. 3D Strain and Elasticity Measurement of Layered Biomaterials by Optical Coherence Elastography based on Digital Volume Correlation and Virtual Fields Method. *Appl. Sci.* **2019**, *9*, 1349. [[CrossRef](#)]
36. Su, Y.; Zhang, Q.; Gao, Z. Statistical model for speckle pattern optimization. *Opt. Express* **2017**, *25*, 30259–30275. [[CrossRef](#)] [[PubMed](#)]
37. Silva, V.B.; Andrade De Jesus, D.; Klein, S.; van Walsum, T.; Cardoso, J.; Brea, L.S.; Vaz, P.G. Signal-carrying speckle in optical coherence tomography: A methodological review on biomedical applications. *J. Biomed. Opt.* **2022**, *27*, 030901. [[CrossRef](#)] [[PubMed](#)]